

Kinematics of earthflows in the Northern California Coast Ranges using satellite interferometry



Alexander L. Handwerger^{a,*}, Joshua J. Roering^a, David A. Schmidt^b, Alan W. Rempel^a

^a Department of Geological Sciences, University of Oregon 1272 University of Oregon, Eugene, OR 97403-1272, USA

^b Department of Earth and Space Sciences, University of Washington, 4000 15th Ave NE, Seattle, WA 98195-1310, USA

ARTICLE INFO

Article history:

Received 5 January 2015

Received in revised form 31 May 2015

Accepted 2 June 2015

Available online 6 June 2015

Keywords:

Slow-moving landslides

Earthflows

Eel River, CA

InSAR

ABSTRACT

Slow-moving landslides exhibit persistent downslope motion with variations in velocity driven by transient stress perturbations along the sliding surface. Here, we use satellite InSAR and high-resolution topographic data to identify 50 slow-moving landslides in the Northern California Coast Ranges, and monitor their seasonal kinematics over 4 years. These landslides have similar mechanical properties and are subject to the same external forcings, which allows us to explore geometrical controls on kinematics. To overcome errors associated with large deformation gradients we incorporate a deformation model in the InSAR processing that enables us to generate deformation time series. We test our novel methodology using a synthetic deformation time series, confirming our ability to resolve seasonal velocity patterns. Time series analysis of four representative landslides reveals that seasonal velocity changes are characterized by comparatively rapid acceleration and gradual deceleration. Each slide displays distinct kinematic zones with different mean velocities, although velocity changes appear to occur synchronously along the landslide body over seasonal timescales. Because these deformation patterns are sensitive to subsurface geometry, we employ a commonly used non-Newtonian viscous flow law to infer slide thickness and find that these slides likely exhibit a highly variable thickness and an irregular (i.e. rough and non-planar) basal sliding surface. Our results suggest that slide geometry controls long-term motion, but does not strongly regulate their response to seasonal stress perturbations.

© 2015 Elsevier B.V. All rights reserved.

1. Introduction

Slow-moving landslides exhibit persistent downslope motion with variations in velocity driven by transient stress perturbations (Terzaghi, 1951; Iverson, 1986; Iverson and Major, 1987; Malet et al., 2002; Schulz et al., 2009a). These stress perturbations alter both the frictional resistance and driving stress along the sliding surface, and can induce complex time-dependent motion along the landslide body. Observations from slow-moving landslides around the world show that differences in motion occur over daily (Van Genuchten and De Rijke, 1989; Schulz et al., 2009a), seasonal (Kelsey, 1978; Iverson and Major, 1987; Coe et al., 2003; Hilley et al., 2004; Calabro et al., 2010; Handwerger et al., 2013), and multi-year timescales (Bovis and Jones, 1992; Mackey and Roering, 2011; Prokešová et al., 2014). Furthermore, the duration and magnitude of motion can vary along the slide body (Baum et al., 1993; Malet et al., 2002; Coe et al., 2003). These behavioral differences reflect how slow-moving landslides respond to changes in stress over a variety of spatial and temporal scales.

In this manuscript we focus on the kinematic evolution of slow-moving landslides in response to seasonal variations in precipitation.

Slow-moving landslides regularly exhibit seasonal velocity patterns, yet it remains unclear how periods of seasonal motion evolve along a landslide body throughout the year. For instance, in some years, periods of acceleration can initiate in isolated zones and propagate along the slide body (referred to as “unsteady, nonuniform motion”), while in other years acceleration can occur simultaneously along the entire slide body (referred to as “unsteady, uniform motion”) (Iverson, 1986; Coe et al., 2003). Given observations outlining the diverse nature of slide behavior, what is the prognosis for predicting how landslides respond to transient changes in stress? In one case, a landslide forced by local or boundary perturbations like headscarp slumping, toe erosion, or local groundwater changes may display progressive motion that travels along the landslide body (Iverson, 1986). By contrast, spatially extensive stress perturbations resulting from changes in the seasonal groundwater level may induce spatially extensive velocity changes. To help differentiate these scenarios, Iverson (1986) developed a quantitative framework to predict how both local and spatially extensive stress perturbations are communicated along a slow-moving landslide. According to his framework, local stress perturbations induce unsteady, nonuniform motion that spreads along the landslide body and spatially extensive stress changes produce unsteady, uniform motion. These model predictions agree with field-based observations made at the Aspen Grove landslide in Utah and the Slumgullion landslide in Colorado (Baum et al., 1993; Coe et al., 2003). Baum et al.

* Corresponding author.

E-mail address: handwerg@uoregon.edu (A.L. Handwerger).

(1993) found that the main body of the Aspen Grove landslide responded to snowmelt weeks before the toe, and the main body continued moving for a month after motion in the toe had ceased. Similar observations were made at the Slumgullion landslide during one year; however, during other years the landslide displayed a more synchronous response to snowmelt. Coe et al. (2003) attributed these disparate behaviors to spatial variations in snowmelt and groundwater levels (i.e. local stress perturbations), which can fluctuate across a single landslide.

Landslide geometry also exerts significant control on landslide motion and dictates how stresses are communicated along the slide body (Iverson, 1986; Baum and Fleming, 1991; Van Asch et al., 2006; Coe et al., 2009; Guerriero et al., 2014; Prokešová et al., 2014). For instance, slope and thickness can vary along an individual landslide such that there is a heterogeneous distribution of shear stress along the slide base. Along a number of landslides, surface measurements are complemented by observations from boreholes and seismic data that map irregularities in the basal slip surface (Mizuno, 1989; Baum and Johnson, 1993; Coe et al., 2009; Guerriero et al., 2014; Prokešová et al., 2014). These irregularities can be used to explain commonly observed surface deformation features and potential controls on the long-term kinematics of these slope failures (Baum and Fleming, 1991; Baum and Johnson, 1993; Coe et al., 2009; Guerriero et al., 2014; Prokešová et al., 2014). By measuring the spatial kinematics of multiple slow-moving landslides subject to the same environmental and tectonic forcing, we can characterize how stresses are communicated along landslide bodies, attempt to discriminate between the effects of local and spatially extensive stress perturbations, and better understand the geometrical controls on landslide motion, including spatial variations in the measured slope and inferred thickness.

Here, we use satellite InSAR with data from the Advanced Land Observing Satellite 1 (ALOS-1) and high-resolution topographic data, including airborne lidar, to identify slow-moving landslides in the Northern California Coast Range and monitor their kinematics between February 2007 and January 2011. Because these landslides have similar mechanical properties (i.e. lithology) and are subject to the same external forcings (i.e. climate, incision), we are able to explore interactions between landslide geometry and kinematics. This builds upon the results of previous work by Handwerger et al. (2013) in which they quantified the velocity time series and seasonal response times (i.e. time lag between rainfall and acceleration) for the fastest moving zones of 10 landslides (a subset of these slides will be discussed below) in order to test predictions of a commonly used hydrological model. In this contribution, we 1) develop and test novel InSAR processing methods that are necessary to construct time series inversions of these landslides, 2) perform a reconnaissance-level survey to identify actively moving landslides across a ~14,000 km² area, 3) examine, for the first time in a regionally extensive study, the spatial and temporal evolution of discrete kinematic zones along landslides that are subject to seasonal changes in effective normal stress, and 4) infer patterns of thickness changes and basal topographic variations using a non-Newtonian viscous flow law.

2. Slow-moving landslides

Slow-moving landslides commonly occur in tectonically active regions with mechanically weak, clay-rich soils, and highly seasonal precipitation. In these areas, they have a profound impact on landscape evolution because they control relief, widen valley spacing, modify drainage patterns, and set hillslope morphology (Kelsey, 1978; Booth et al., 2013b; Simoni et al., 2013). They occur in a small fraction (<10%) of the landscape, and contribute a large fraction (up to 50%) of the regional sediment flux (Kelsey, 1978; Mackey and Roering, 2011; Simoni et al., 2013). These slope failures tend to span from hilltop to channel bottom creating kilometer-scale planar hillslopes with gentle topographic gradients (Keefer and Johnson, 1983; Booth and Roering, 2011). All of these factors combine to leave a distinct topographic signature on the landscape, which can be identified through quantitative analysis of high-resolution DEMs (Booth and Roering, 2011; Booth et al., 2013b). Additionally, slow-

moving landslides are a major natural hazard, and although they seldom fail catastrophically, they cause significant damage to infrastructure.

Here, we focus on large (km-scale), deep-seated (>5 m), slow-moving (m yr⁻¹) landslides often called earthflows (Keefer and Johnson, 1983; Hungr et al., 2001; Mackey and Roering, 2011). Although these slides display a flow-like surface morphology, most movement occurs by frictional sliding along discrete shear surfaces. In this manuscript, we use the terms landslide, slide, slow-moving landslide, and earthflow interchangeably. Earthflows exhibit a wide range of sizes and shapes, but they are most often identified by a hummocky surface, and hourglass planform (Keefer and Johnson, 1983; Mackey and Roering, 2011; Simoni et al., 2013). Their spatial dimensions can range over two-to-three orders of magnitude, with the largest slides reaching up to several kilometers in length, hundreds of meters in width, and tens of meters in thickness. Although their planform areas are relatively easy to delineate with field-observations and high-resolution DEMs, their thicknesses are often poorly constrained because most measurements of landslide thickness come from individual boreholes, hillslope-channel interfaces, or gullies incised through the landslide body, which in many cases do not intersect the basal shear zone. Recent work has been aimed at developing depth-area scaling relationships for earthflows and has found that they tend to be slightly deeper relative to their area when compared to other types of landslides composed of unconsolidated materials (Larsen et al., 2010; Handwerger et al., 2013; Simoni et al., 2013).

Other studies have used measurements of surface deformation to infer the subsurface geometry of slow-moving landslides (Baum et al., 1993; Coe et al., 2009; Guerriero et al., 2014). Recently, Guerriero et al. (2014) used surface deformation features (e.g., cracks, faults, tilted surfaces) and the location of spatially fixed ridges and depressions (e.g., sag ponds, springs) on the ground-surface to infer basal topography. They confirmed their results with numerous borehole measurements and seismic data. Several studies have also used 2-D and 3-D mass conservation techniques to estimate changes in landslide thickness (e.g., Bishop, 1999; Booth et al., 2013a). Each of these studies has concluded that slow-moving landslides have an irregular (i.e. non-planar and rough) basal-slip surface and exhibit significant changes in thickness across the landslide body. These findings have major implications for field instrumentation design and mitigation strategies (Hutchinson, 1970), estimates of landslide volume, and for the development of slope stability models, which most often assume a smooth and listric or planar shear surface. Furthermore, the form of this basal interface may be a primary control on pore-water pressure-deformation feedbacks (Baum and Johnson, 1993; Van Asch et al., 2006).

Earthflows exhibit nearly plug-flow deformation by sliding along basal and lateral shear zones, often with minimal internal deformation. Observations from borehole inclinometers reveal that the majority of the shear deformation is accommodated along millimeter- to meter-scale shear zone thicknesses, while the near surface translates like a rigid block (Swanson and Swanston, 1977; Vulliet and Hutter, 1988; Simoni et al., 2013). This behavior can be approximated by a viscous flow model with a non-Newtonian rheology. Using this approach, several studies have successfully modeled earthflows over both short and long timescales (Vulliet and Hutter, 1988; Booth et al., 2013b). Most recently, Booth et al. (2013b) parameterized a viscous flow model using borehole inclinometer data from multiple earthflows around the world and incorporated it into a landscape evolution model that was able to reproduce many of the key topographic features (e.g., relief, topographic slope, valley spacing) of earthflow-dominated landscapes.

Earthflows are often partitioned into three main kinematic zones, namely: the head, transport, and toe zones. Velocities tend to be highest through the transport zone and decrease towards the head and toe zones. The spatial locations of these kinematic zones remain fixed over long time periods (~10¹–10² years), which suggests that these regions are set by the hillslope and landslide geometry (Coe et al., 2009; Mackey et al., 2009; Guerriero et al., 2014). Average slide velocities range from a few decimeters to several meters per year, but can be

variable over daily-to-decadal timescales (Iverson and Major, 1987; Bovis and Jones, 1992; Schulz et al., 2009a; Mackey and Roering, 2011; Handwerger et al., 2013; Prokešová et al., 2014).

Seasonal velocity changes are driven by hydrologic forcing, like rainfall and snowmelt, that acts to increase pore-water pressure along the shear zone, which reduces frictional resistance and triggers acceleration (Terzaghi, 1951; Iverson and Major, 1987; Coe et al., 2003; Handwerger et al., 2013). Deceleration begins as pore-water pressures decline due to drainage, precipitation decreases, and potentially as a result of other mechanical feedbacks like granular dilation (Iverson, 2005; Schulz et al., 2009b) or frictional rate-strengthening (Wang et al., 2010). In contrast to shallow landslides, which are often triggered by short periods of intense precipitation, deep-seated earthflows typically require longer (i.e. seasonal) periods of precipitation to increase pore-water pressures in the basal shear zone to levels that trigger detectable motion (Iverson and Major, 1987). Field-based measurements and numerical models have shown that transient variations in pore-water pressure diffuse vertically from the ground surface to the basal shear zone (Iverson and Major, 1987; Haneberg, 1991; Reid, 1994; Baum and Reid, 1995; Berti and Simoni, 2010; Berti and Simoni, 2012). This theoretical framework implies that for landslides with similar precipitation, material properties, and topographic slopes, the amount of time required for pore-water pressure changes to occur in the basal shear zone should scale with the slide thickness. However, Handwerger et al. (2013) found that the transport zones for 10 slow-moving landslides (a subset of the same slides discussed in this study) that vary by a factor of 5 in estimated thickness respond to seasonal precipitation with a remarkably similar timing and magnitude. This observation either contradicts the predictions of the simple 1D diffusion model or provides evidence that the effective hydraulic parameters are outside the range of commonly assumed values for clay-rich soils. In addition, the lateral (i.e. downslope) transmission of pore-water pressure may be important in triggering landslide motion (Priest et al., 2011).

3. Study area: Northern California Coast Range

Our InSAR study covers an area of ~14,000 km² in the Northern California Coast Ranges (Fig. 1). In particular, we focus on the mainstem of the Eel River, which is well known for its earthflow activity and has been the focus of many landslide investigations in recent years (Roering et al., 2015). The Northern California Coast Range is a tectonically active mountain belt that extends northwest from the San Francisco Bay to the Oregon border. The region has a Mediterranean climate with cool, wet winters and hot, dry summers. Average annual rainfall is 1.4 m yr⁻¹, falling mostly between October and April and reaching peak rates between December and February. Vegetation is a mixture of open oak grassland and conifer forest.

The Coast Range is composed of the Jurassic–Cretaceous Franciscan Complex, a pervasively sheared accretionary prism that has been uplifting since the Miocene. The Franciscan Complex is separated into three distinct structural belts that decrease in age to the West, named the Coastal, Central, and Eastern belts (Jayko et al., 1989; McLaughlin et al., 2000). The Central belt, which is particularly susceptible to earthflow-style landslides, is comprised of an argillaceous mélange matrix surrounding more coherent blocks of sandstone, chert, shale, and older metamorphosed units (e.g., meta-basalt, blueschist) inherited from the Eastern belt. These coherent blocks play an important role in the evolution of this landscape because they influence the local hillslope gradient, impact earthflow behavior, create river knickpoints, and have the potential to fail as large, catastrophic, river-damming landslides (Mackey et al., 2011).

Due to its high erosion rates, the Eel River catchment has been widely studied since the late 1960s. Brown and Ritter (1971) found that the Eel River had the highest average sediment yield per drainage area of any non-glacial or volcanic river in the conterminous United States. Since then, many studies have quantified erosion rates using a variety of tools, including suspended sediment and hydrologic data (Wheatcroft and Sommerfield, 2005) and cosmogenic radionuclides (Fuller et al., 2009;

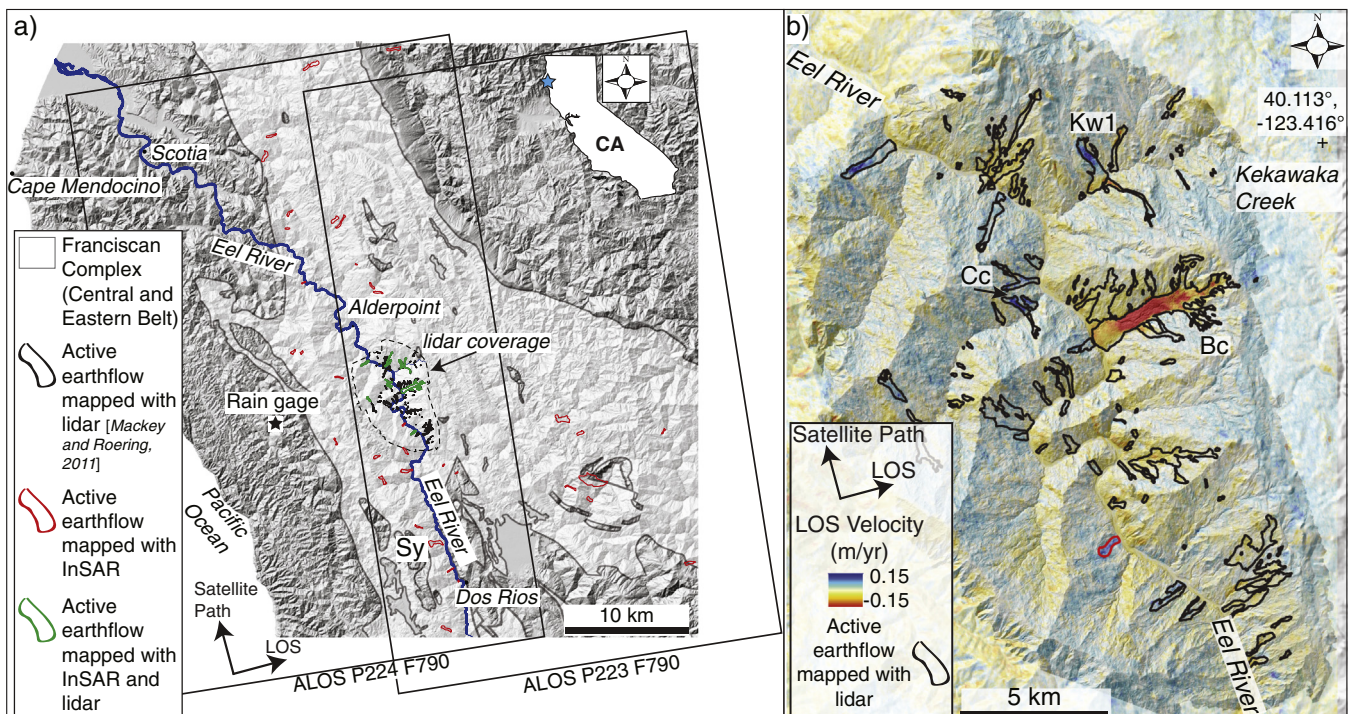


Fig. 1. Landslide inventory. a) Hillshade map of Northern California Coast Range field site. Black rectangles outline ALOS-1 PALSAR data coverage for satellite paths 223-F790 and 224-F790. Thick blue line highlights the mainstem of the Eel River. Light gray area outlines the Eastern and Central belts of the Franciscan Complex (Jennings et al., 1977). Inset in upper right corner shows California with blue star marking the location of the field area. Black star marks location of NOAA rain gage. b) A 46-day interferogram stack draped over lidar hillshade. Positive velocity values correspond to motion away from the satellite along the line-of-sight. Black polygons show previously mapped earthflows (Mackey and Roering, 2011). Earthflow names indicate the slides examined in our time series analysis and are abbreviated as the following: Bc = Boulder Creek, Cc = Chamise Creek, Sy = Simmerly Road, and Kw1 = Kekawaka Creek 1. (For interpretation of the references to color in this figure legend, the reader is referred to the web version of this article.)

Balco et al., 2013; Roering et al., 2015). Each of these studies has corroborated the catchment's high erosion rates, with values from 0.3 to 1.1 mm yr⁻¹. The majority of the total erosion can be directly attributed to active landsliding. Kelsey (1978) and Mackey and Roering (2011) found that active earthflows contribute up to 50% of the regional sediment flux to channels.

Although many studies have investigated erosion rates in our field area, estimates of rock uplift are sparse and indirect (Furlong and Govers, 1999; Lock et al., 2006). The Northern California Coast Range is actively uplifting due to crustal thickening and dynamic topography resulting from the northward passage of the Mendocino Triple Junction (MTJ). Geomorphic evidence (e.g., river capture, drainage reversal) (Lock et al., 2006) and a geodynamic model (Furlong and Govers, 1999) suggest that this region is experiencing a double-humped zone of rock uplift that is riding along with the MTJ. If true, this pattern of rock uplift may have implications for the frequency and magnitude of landslides (Roering et al., 2015). Predicted estimates of uplift near our field area, which is roughly 100 km E–SE of the MTJ, range from 0.5 to 1 mm yr⁻¹ (Lock et al., 2006). Additional estimates of rock uplift from marine terraces in the King Range, which is much closer to the MTJ, approach 5 mm yr⁻¹ (Merritts and Bull, 1989); however, the King Range is regarded as a tectonically distinct region and uplift rates are known to decay inland, coincident with a shear zone that surrounds the range (McLaughlin et al., 2000; Lock et al., 2006).

4. Methodology

The dynamics of slow-moving landslides are governed by complex mechanical–hydrological interactions between landslide properties and external forcings (e.g., precipitation, incision). Unraveling these interactions requires high-resolution spatial and temporal observations from well-chosen sites that allow for some landslide properties to be varied (e.g., geometry) while most are held constant (e.g., climate, tectonics, material properties). Recent advances in remote sensing techniques, like satellite radar interferometry (InSAR), now enable high-resolution spatial and temporal measurements that can quantify the kinematic history along multiple landslides subject to nearly identical environmental forcings. The resulting constraints can be used to quantify how landslide geometry influences slide behavior.

In the past two decades, InSAR has become a well-established technique for monitoring landslide displacement, taking advantage of the increased availability of SAR data from multiple satellites and the development of advanced processing techniques, such as permanent scatterers InSAR (PS-InSAR) (Ferretti et al., 2001; Colesanti and Wasowski, 2006). There are now SAR data available from more than 10 satellites, spanning over two decades, and covering almost the entire globe. In addition, ground-based and Uninhabited Aerial Vehicle (UAV) radar interferometers are becoming more common, both of which allow for highly targeted investigations (Schulz et al., 2012; Lowry et al., 2013; Scheingross et al., 2013).

While numerous studies have used InSAR to construct regional landslide inventories (Zhao et al., 2012; Scheingross et al., 2013), assess potential hazards (Castañeda et al., 2009), and examine the kinematics of individual slides (Calabro et al., 2010), few have compared and contrasted the time-dependent displacement of multiple neighboring landslides (Hilley et al., 2004; Handwerger et al., 2013). This is likely a result of the high quantity of interferograms required to construct InSAR time series inversions (Schmidt and Bürgmann, 2003), which can be difficult to attain because InSAR studies in landslide-prone areas are often challenged by large deformation gradients, steep and vegetated topography, the one-dimensional viewing geometry of the satellite, and atmospheric noise from frequent precipitation (Colesanti and Wasowski, 2006).

Here, we use conventional 2-pass InSAR to quantify the kinematics of slow-moving earthflows in the Northern California Coast Range. Previous studies using InSAR in this region have demonstrated the capability of

the method to identify and monitor multiple active landslides that span an order of magnitude in size and velocity (Roering et al., 2009; Zhao et al., 2012; Handwerger et al., 2013). The Northern California Coast Range is an ideal location for using conventional 2-pass InSAR because earthflow motion is fast enough to observe over a short time period and slow enough to avoid radar decorrelation. Although these earthflows are particularly well suited for conventional InSAR techniques, their persistent downslope motion is problematic for producing long-duration interferograms because conventional InSAR requires that the change in the phase from one pixel to the next be $< 2\pi$ radians (< 11.75 cm for ALOS-1). Since many of the landslides in our field area are moving on the order of m yr⁻¹, deformation associated with long-duration (> 46 days) interferograms often exceeds this phase-change threshold and the deforming area becomes decorrelated or contains unwrapping errors (Stimely, 2009). In Section 4.3, we describe a scalable deformation model, which allowed us to overcome these limitations so that we can produce deformation time series and explore geometrical controls on landslide kinematics.

4.1. InSAR methodology

We use conventional 2-pass InSAR with data from the ALOS-1 satellite to identify active earthflows between February 2007 and January 2011. SAR data were acquired with the PALSAR instrument, which operates with an L-band antenna (23.6 cm wavelength) and a 46-day repeat interval. This satellite has a look direction of 075° (east of North) and incidence angle of 34.3° from vertical. Our study area is covered by overlapping satellite path 223 frame 790 (P223) and path 224 frame 790 (P224) (Fig. 1a), whose data acquisition times are offset by a few weeks (Table S1). Due to technical issues, the ALOS-1 satellite was decommissioned in May 2011.

We produced 81 differential interferograms using 17 scenes from P223, and 21 scenes from P224 (Table S1). Interferograms were processed with the Repeat Orbit Interferometry Package (ROI PAC) developed at JPL/Caltech (Rosen et al., 2004). We used a 1 arc-sec (30 m resolution) DEM from the Shuttle Radar Topography Mission (SRTM) (Farr et al., 2007) to remove topographic contributions to the phase. SAR data were processed at 4-looks in range and 20-looks in azimuth, and resampled at the resolution of the DEM upon orthorectification (~ 30 m pixel). To reduce noise, we used a power spectral filter value between 0.1 and 0.3 (Goldstein and Werner, 1998). Although other SAR satellites (e.g., ERS1/2, ENVISAT, RADARSAT) cover a longer time period and have shorter repeat intervals than ALOS-1, attempts to image landslide deformation with these C-band (5.6 cm) satellites were unsuccessful, likely because their shorter wavelength could not sustain coherence in our vegetated study area (Stimely, 2009).

4.2. Landslide reconnaissance using InSAR

To identify active landslides, we performed a reconnaissance-level investigation of both satellite paths by stacking interferograms (i.e. time-averaged deformation) and using statistical analysis to discriminate deformation from artifacts. Stacking increases the signal-to-noise ratio and highlights features that are persistent in time and space. We found that patches with high line-of-sight (LOS) velocity and high standard deviation of LOS velocity are effective criteria for identifying active slides. In addition, we overlaid the InSAR stacks onto a shaded relief map to verify that these patches correspond to landslide topography (Fig. 1b). To directly compare landslides to each other and to previous studies, we back-projected LOS velocity onto the downslope direction using a vector projection (see Appendix A). We use both LOS velocity and downslope velocity to analyze data in the forthcoming sections. Lastly, to quantify the spatial attributes of each slide we used high-resolution DEMs generated from lidar (1 m pixel) and from the USGS National Elevation Dataset (10 m pixel) (Gesch et al., 2002).

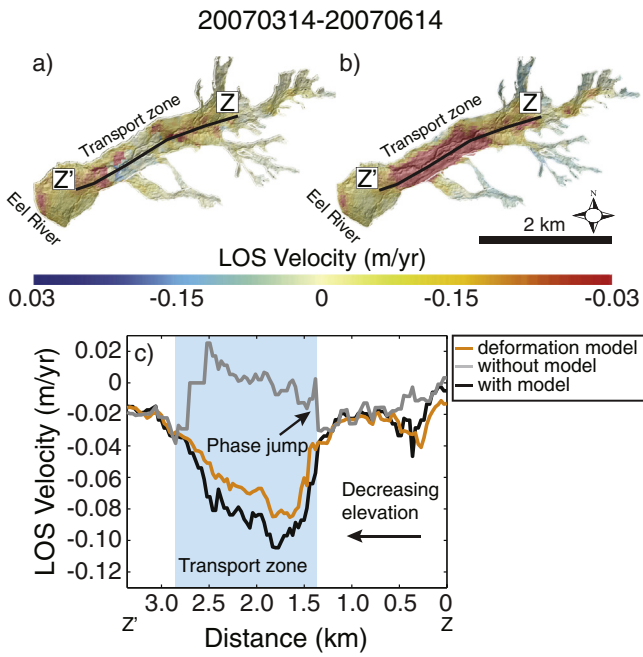


Fig. 2. A 92-day interferogram of the Boulder Creek earthflow draped on lidar hillshade. Positive velocity values correspond to motion away from the satellite along the line-of-sight. The color scales are saturated such that the actual velocity values (m yr^{-1}) exceed the maximum and minimum listed values. a) LOS velocity map processed without deformation model. Interferogram processed without the deformation model contains a phase jump due to an unwrapping error that is caused by the large deformation gradient at the margin of the transport zone. b) LOS velocity map processed with deformation model. c) LOS velocity profile from Z to Z' using values from a) and b) and the deformation model. Shaded area marks the spatial location of the transport zone. (For interpretation of the references to color in this figure legend, the reader is referred to the web version of this article.)

4.3. Deformation model for processing long-duration interferograms

The persistent downslope motion of the Eel River slides is problematic for producing long-duration (>46 days) interferograms. By using a deformation model, which is subtracted from the raw interferogram, we are able to maintain coherence and minimize unwrapping errors for interferogram durations up to 276 days. The model is constructed from a stack of 46-day interferograms for each individual landslide that is scaled to the duration of the interferogram being processed. In other words, if we are processing a 92-day interferogram, we multiply the deformation model by a factor of 2. Thus, the model represents the average deformation of each landslide over the specified time period. This allows us to recover deformation beyond the scaled deformation model by maintaining coherence (Bürgmann et al., 2006; Wei

et al., 2010; Tong et al., 2013). After the interferogram is filtered and unwrapped, the deformation model is added back into the interferogram and processing proceeds. This technique works well because it prevents the phase gradient from exceeding 2π radian (11.75 cm) per pixel (the threshold where coherence is lost), while allowing for the residual deformation to be processed (Fig. 2). We have carefully compared the unwrapped interferograms to the original unfiltered wrapped interferograms to ensure that no artifacts are introduced by this process (Fig. S1).

4.4. InSAR time series

InSAR is capable of resolving complex time-dependent deformation patterns if redundant data can be used to differentiate signal from noise (Schmidt and Bürgmann, 2003). This requires a temporally rich dataset with multiple interferograms that overlap in time. To increase both the temporal resolution and number of interferograms used in the inversion, we selected four landslides that lie within the overlapping regions of satellite paths 223 and 224 (Fig. 1a). We do not compensate for the slightly different look angle for common pixels on overlapping paths. We forward calculate the change in phase that results from differences in the look angle and estimate that this introduces a LOS error of <5%. Using the method of Schmidt and Bürgmann (2003), we calculated the velocity time series for the four landslides by performing a linear least-squares inversion of 51 independent, unwrapped interferograms (Table S2). In order to minimize topographic contributions to the phase and to preserve nearly complete spatial coverage of each landslide, we selected interferograms with short spatial baselines (<1400 m) and minimal decorrelation. We are unable to process interferograms during summer 2008 because of an issue with the satellite acquisition system that produced unusually large spatial baselines and resulted in completely decorrelated interferograms.

4.5. Synthetic deformation time series

Because we have no complementary measurements of seasonal landslide motion to compare against our InSAR time series results, we constructed a synthetic deformation time series to rigorously test our time series methodology and to identify potential sampling biases. Our synthetic time series was made using simulated SAR scenes with two populations of pixels. One population of pixels was made using a simple surface-displacement model to simulate general patterns of earthflow motion over the 4-year study period. The other population of pixels used in the simulated SAR scenes experienced no deformation and was used as a stable reference point in the time series inversion. We define the surface displacement model using

$$D = \bar{V}t + A \sin(2\pi t/\lambda) \tag{1}$$

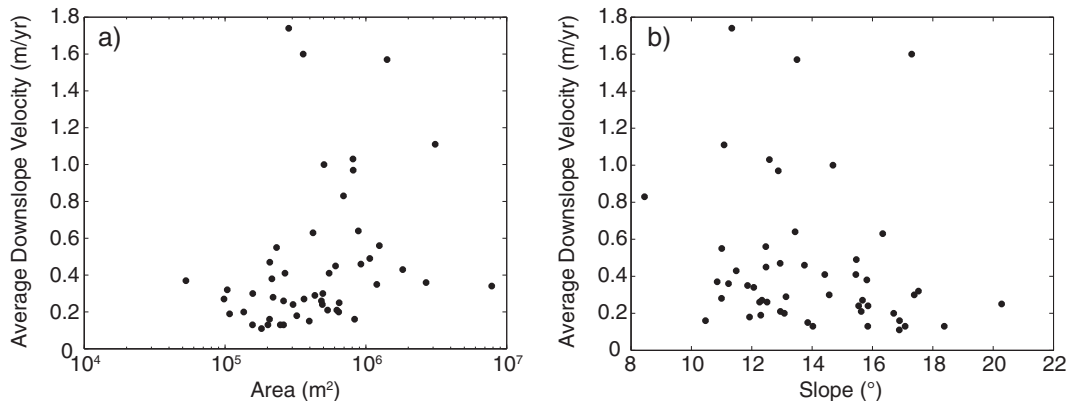


Fig. 3. Projected downslope velocity for 50 slow-moving landslides as a function of a) landslide area and b) average topographic slope. Average slope is measured along the longitudinal axis of each slide. We find no clear relation between average landslide size, average topographic slope, and average slide velocity. See Table S5 for detailed statistics.

where D is the cumulative displacement, \bar{V} is the average annual displacement rate, t is time, A is the sinusoidal wave amplitude (i.e. magnitude of seasonal velocity changes), and λ is the sinusoidal wavelength (i.e.

wavelength of seasonal velocity changes). The linear deformation term and a sinusoidal deformation term are chosen to simulate annual and seasonal displacement, respectively. We tested a wide range of annual

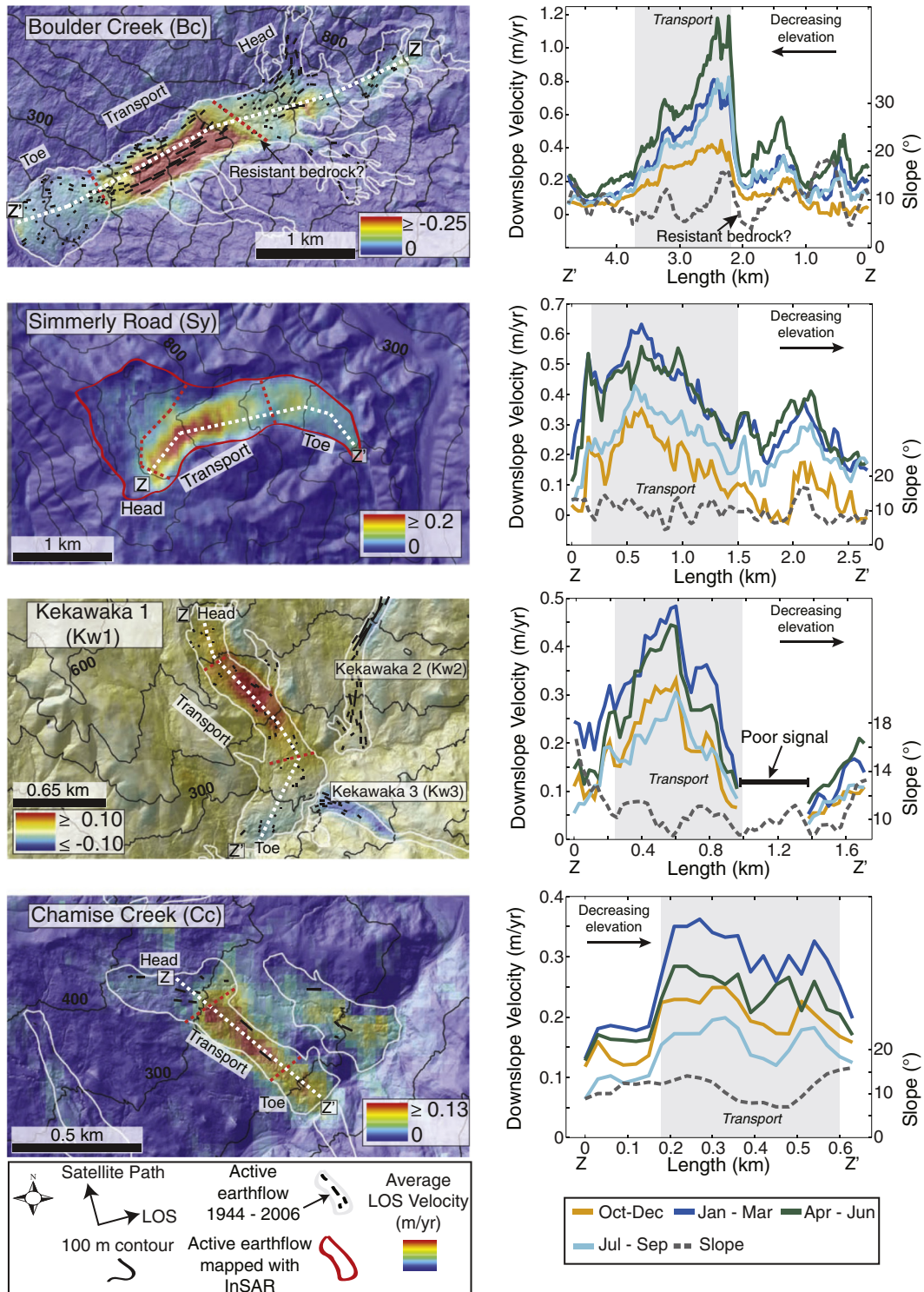


Fig. 4. 4-year averaged interferograms draped over hillshade maps for four representative earthflows modified from Handwerger et al. (2013). Positive velocity values correspond to motion away from the satellite along the line-of-sight. Note that the color scale is reversed for the Boulder Creek earthflow in order to highlight the transport zone with red colors. The color scales are saturated such that the actual velocity values (m yr^{-1}) exceed the maximum and minimum listed values. White polygons show landslide boundaries mapped by Mackey and Roering (2011). Short black lines show landslide motion mapped using historic aerial photos (Mackey and Roering, 2011). Dashed lines along longitudinal axis indicate locations of velocity and topographic slope profiles. Dashed lines perpendicular to longitudinal axis mark location of kinematic zones. Each slide is delineated into head, transport, and toe zones. Profiles from Z to Z' showing topographic slope and seasonally averaged velocity. Shaded area marks the spatial location of the transport zone. The poor signal indicated along the Kw1 slide is explained in Appendix A2. (For interpretation of the references to color in this figure legend, the reader is referred to the web version of this article.)

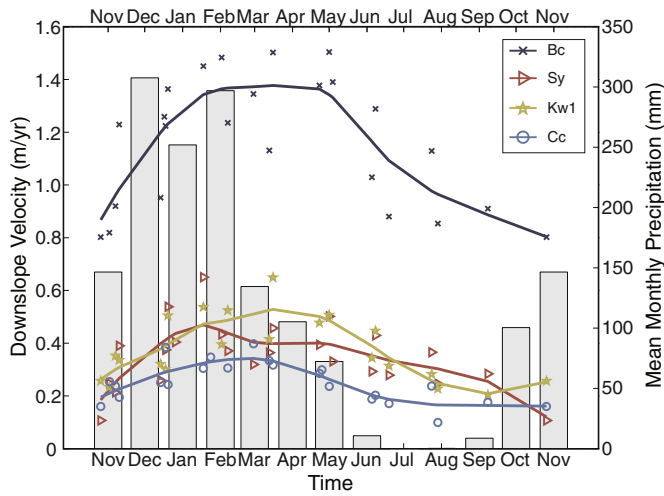


Fig. 5. Velocity time series for the transport zone (spatially averaged) of four earthflows projected onto the downslope direction. Data from March 2007 to January 2011 is condensed into a single calendar year and plotted by day of the year. Symbols represent measured values and lines represent a smooth-spline fit to the data. Gray bars indicate mean monthly precipitation over the same time span. Precipitation data collected at Richardson Grove State Park, CA located ~30 km west of our field area (Fig. 1). Earthflow names are listed in the caption to Fig. 1.

velocities ($\bar{V} = 0.2$ to 2 m yr^{-1}), wave amplitudes ($A = 0.002$ to 0.15 m), and wavelengths ($\lambda = 0.1$ to 4 yr). We also added correlated random noise with a normal distribution (mean = 0 m , std = 0.01 m) to approximate atmospheric artifacts (Lohman and Simons, 2005). The magnitude of our synthetic error source was validated by checking the apparent deformation of areas known to be stable (e.g., hilltops) in our interferograms. The model was sampled to match the temporal distribution of the InSAR dataset and run through the time series inversion.

First, we tested the sensitivity of the inversion to the temporal distribution of interferograms. We found that by using all of the small-baseline interferograms from satellite paths 223 and 224 (“P223–P224 combined”) (Table S1), the inversion output contained high frequency oscillations that were not included in the input model (Fig. S2). This inversion misfit is a result of the high number of SAR scenes relative to the number of interferograms, which can destabilize and decrease the resolution of the inversion (Schmidt and Bürgmann, 2003).

To reduce the misfit error while maintaining high data redundancy, we manually adjusted the acquisition dates of 20 SAR scenes that were collected <20 days apart, to the midpoint date of the acquisitions (“P223–P224 modified”) (Fig. S2; Table S3). For example, SAR scenes with acquisition dates 20090804 and 20090821 were adjusted to 20090812. Because only minor deformation (<2 cm) occurs over the <10 day period (i.e. midpoint of <20 days) this does not affect the seasonal landslide signal. In addition to the individual SAR scenes collected within 20 days of each other, there are 13 interferogram pairs that have acquisition dates <20 days apart (Table S1). For these interferograms, we adjusted their acquisition dates and used the average of their deformation signals. By making this adjustment to the scene acquisition dates, the inversion output did not contain high frequency oscillations and more closely matched the synthetic input signal (Fig. S2). For the remainder of our analysis we use the “P223–P224 modified” distribution of interferograms.

Lastly, we used the synthetic interferograms to determine the minimum detectable seasonal wavelength of our irregularly sampled InSAR dataset. We tested synthetic models with sinusoidal wavelengths ranging from 0.25 to 4 years and found that the misfit decreased nonlinearly with increasing wavelength such that we can resolve seasonal signals with a wavelength ≥ 0.5 years (Fig. S3).

4.6. Non-Newtonian viscous flow model to infer slide thickness

To explore subsurface controls on landslide motion we inferred landslide thickness using a viscous flow model with a non-Newtonian rheology. The viscous flow model provides an approximate relationship between surface velocity, topographic slope, and earthflow thickness at a given pixel i , such that

$$V_i = \frac{(c\rho g S_i)^p H_i^{p+1}}{p+1} \quad (2)$$

where V_i is the downslope velocity, S_i is the sine of the topographic slope-angle, H_i is the earthflow thickness, c is a flow law constant, ρ is the earthflow density, g is the gravitational acceleration, and p is the flow-law exponent (Booth et al., 2013b). Parameter values are listed in Table S4. We rearrange Eq. (2) to write the thickness at each pixel as

$$H_i^{p+1} = \frac{V_i(p+1)}{(c\rho g S_i)^p}. \quad (3)$$

Given velocity values measured with InSAR and slope values measured along the slide axis with DEMs, Eq. (3) can be used to infer continuous profiles of slide thickness.

Before proceeding, it is worth noting that the viscous flow model does not explicitly describe the mechanics of frictional sliding that are believed to be primarily responsible for the observed landslide deformation. This recognition has led to considerable debate over whether it is appropriate to use viscous flow models to characterize landslide (and subglacial deforming till) motion (Hungr, 1995; Iverson, 2005; Iverson, 2010). An attractive feature of the viscous flow model is the clear and simple correspondence predicted between higher driving stresses and faster surface motions. This has enabled such treatments to provide useful characterizations of landslide motion over a variety of spatial and temporal scales (e.g., Vulliet and Hutter, 1988; Booth et al., 2013b). More elaborate frictional treatments that incorporate a rate dependence through considerations of dilatancy and associated pore pressure changes yield predicted landslide behavior that is reported to strongly resemble motion resisted by viscous deformation (Iverson, 2005). Nevertheless, it should be emphasized that our viscous flow model is not intended to reveal precise soundings of flow depth, but instead only to uncover broad patterns of variability in the basal geometry.

5. Results

5.1. Landslide inventory

We identified 50 active landslides across the ~14,000 km² area covered by the two satellite paths (Fig. 1). The landslides have spatial dimensions ranging from 0.4 to 5.4 km long, 0.1 to 1.4 km wide, 0.05 to 7.8 km² in planform area, and have average downslope velocities ranging from 0.1 to 1.7 m yr^{-1} (Table S5). All but one of the 50 earthflows are located within the Central and Eastern belt of the Franciscan Complex (Fig. 1), which indicates a strong lithologic control on their spatial distribution, consistent with the results of Mackey and Roering (2011), who found that the majority of the earthflows in this region occur within a mechanically weak and argillaceous unit of the Franciscan Complex. There is no clear relation between landslide size, average topographic slope, and average velocity (Fig. 3). Each slide has three main kinematic zones which we refer to as the head, transport, and toe zones. Peak velocity values occur in the transport zone and decrease towards the head and toe zones. Fig. 4 displays annotated interferograms, highlighting each kinematic zone, for four representative earthflows. We delineate these zones based on surface velocities and deformational structures identified with the DEM. We expect that these slides can be subdivided into smaller quasi-discrete zones (e.g., Guerriero et al., 2014), but this requires detailed field investigation or multi-temporal high-resolution

DEMs. For the 13 slides that occur within the area of lidar coverage (previously mapped by Mackey and Roering, 2011), we observe a similar average annual velocity and find that the kinematic zones have remained spatially fixed since at least 1944, suggesting that the locations of these zones are primarily set by the landslide geometry. These earthflows also display cross-slide variations in velocity, which confirms a flow-like (i.e. lateral strain) component (Fig. 4).

It is important to note that InSAR is blind to deformation that occurs along the satellite's flight path and any landslides with dominant motion in the NW–SE direction remain undetected (see Appendix A2). In addition, there is a bias towards larger and slower landslides because smaller and faster slides (e.g., debris flows) cover only a few pixels of the InSAR data and are limited by deformation thresholds. Therefore, our landslide inventory provides a minimum estimate of the total number of active landslides in this region between 2007 and 2011.

5.2. Velocity time series

We calculated the velocity time series for four representative earthflows that lie within the overlapping regions of satellite paths 223 and 224 and have minimal decorrelation (Fig. 4). By combining SAR data from both satellite paths we have achieved a temporal sampling ranging from 29 to 193 days with a mode of 46 days (Table S2). These earthflows range in area from 0.16 to 3.1 km², estimated average thickness from 15 to 40 m, and average downslope velocity from 0.3 to 1.2 m yr⁻¹. To characterize general patterns of seasonal motion, we collapsed the 4-years of InSAR data from the transport zone of each slide

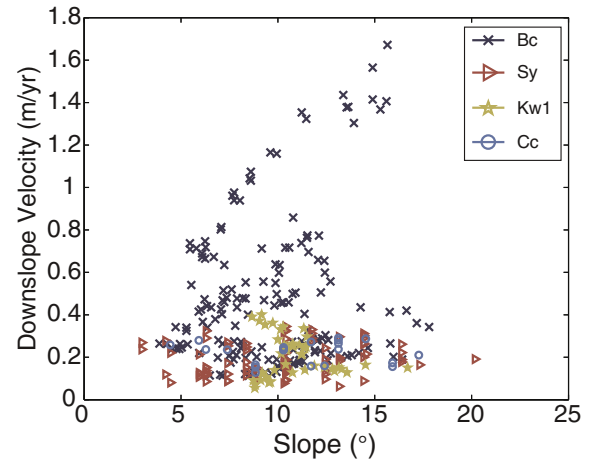


Fig. 7. Topographic slope versus temporally averaged downslope velocity. Each symbol corresponds to the slope–velocity relationship at an individual pixel along the slide axis. Slope–velocity values are taken along the profiles shown in Fig. 4. The Boulder Creek earthflow appears to have the strongest correlation between slope and velocity.

into a single calendar year and plotted their velocity by day of the year (Fig. 5). Consistent with the regional precipitation patterns, the slides exhibit well-defined seasonal velocity changes that are characterized by relatively short periods of acceleration lasting ~30% of the year, followed by longer periods of deceleration lasting ~70% of the year (Fig. S4). Each earthflow accelerates smoothly to wet-season rates,

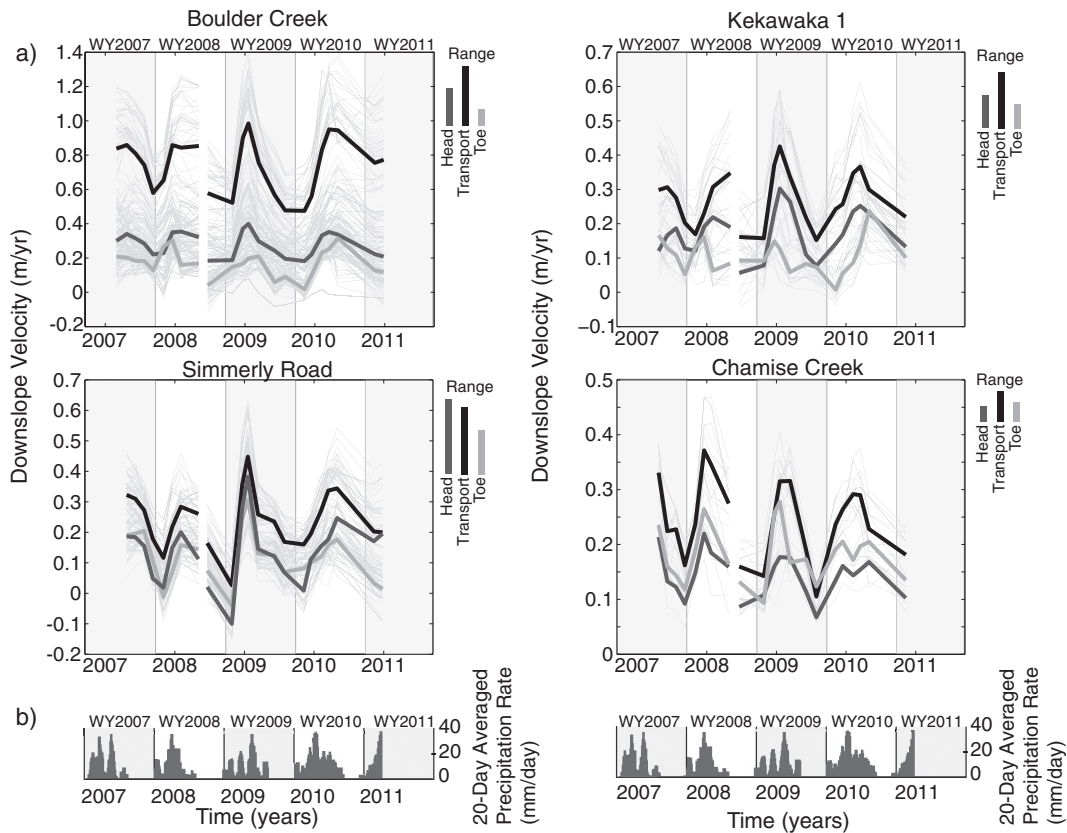


Fig. 6. Velocity time series along the longitudinal axis of each landslide. a) Projected downslope velocity time series between February 2007 and January 2011. Thin gray lines represent the velocity time series for each pixel along the longitudinal profiles in Fig. 4. Thick lines indicate spatially averaged values of each kinematic zone. Transport zone lines are modified from Handwerger et al. (2013). Range bars represent the relative range of scatter in the data for each kinematic zone. Data gap over summer 2008 results from decorrelated interferograms. b) 20-day averaged precipitation rate. Precipitation data collected at Richardson Grove State Park, CA located ~30 km west of our field area (Fig. 1). Gray and white boxes and dashed lines correspond to alternating water years (WY). WY is defined as Oct 1–Sept 30. We observe that the head, transport, and toe regions accelerate in unison across the slide. Note temporal offsets and negative velocity values occur in low velocity regions of some slides. We attribute these offsets and negative velocities to inversion misfit resulting from a low signal-to-noise ratio (i.e. low velocity).

lagging the onset of rainfall by a maximum of 1 to 2 months (Handwerger et al., 2013), and then decelerates smoothly to dry-season rates. We observed no true steady-state motion over the 4-year study.

Next, we analyzed seasonal kinematics along the longitudinal axis of the four earthflows. To examine how the seasonal velocity changes occur within each kinematic zone, we binned the velocity time series data into 3-month intervals starting at the onset of seasonal rainfall in October (Fig. 4; Fig. S5). All parts of the slide, to the sub-kinematic zone scale, display seasonal velocity changes that scale in proportion throughout the year. That is, the fastest moving region remains as such in both wet and dry seasons. We also observe distinct differences in seasonal sliding rate between each kinematic zone. Transport zone rates can exceed the head and toe zone rates by a factor of 4, while the head and toe zone rates are within a factor of 2. Although the transport zone maintains persistent downslope motion year round, during the dry season the head and toe zones either come to a halt or move too slowly ($< \text{cm yr}^{-1}$) for InSAR to detect significant motion.

We also analyzed the timing of these seasonal velocity changes in an attempt to differentiate between uniform and nonuniform motion. It appears that the majority of the seasonal velocity changes occur concurrently along the slide body (Fig. 6; Video S1), suggesting that changes in effective normal stress are spatially extensive over observed timescales. Our analysis is limited by the temporal sampling of our InSAR dataset, which is somewhat irregular (Table S2), and we are unable to detect changes in deformation rate that occur between satellite acquisitions (mode of 46 days). Furthermore, our analysis of the slowest moving parts of the landslides is affected by a low signal-to-noise ratio that may enhance errors. For example, the analysis appears to indicate a temporal offset in motion and even slight negative velocity values (i.e. upslope motion) along the slowest-moving parts of the toe zones for Boulder Creek during 2007 and for Kekawaka 1 during 2007 and 2010 (Fig. 6). Given the limitations in the InSAR data, we cannot exclude the possibility that local stress perturbations are either triggering seasonal motion that propagates along the landslide body or triggering variations in motion over even shorter timescales. We calculate that if motion is triggered by local stress perturbations, the instability must travel along the landslide body at 10^2 – 10^3 m day $^{-1}$, which is several orders of magnitude faster than the average landslide velocity.

5.3. Topographic slope, surface velocity, and inferred thickness

We did not find any clear correlation between average topographic slope and average slide velocity for these earthflows (Fig. 3); however,

local changes in slope and thickness (i.e. driving stress) control slide velocity. By comparing slope and velocity over small spatial scales along the slide axis (30 m pixels), we find that, in some areas, changes in topographic slope are strongly correlated to changes in slide velocity, while in other areas there is weak to no correlation (Fig. 4). Also, for a given slope value there is a relatively wide range in velocity values (Fig. 7).

Assuming these earthflows can be approximated as viscous flows with a non-Newtonian rheology, our observations suggest that the thickness of these earthflows must be highly variable to explain their slope–velocity relationship. Using Eq. (3), we estimated the changes in slide thickness required to explain the slope–velocity values at the Boulder Creek earthflow. We only present data from Boulder Creek, but this analysis can be applied to each of the slides that have an InSAR signal with a high signal-to-noise ratio. Given the parameters listed in Table S4, Eq. (3) predicts a highly variable thickness with values ranging from 14 to 44 m (Fig. 8). These inferred thickness values are within the range of thickness estimates made by Mackey and Roering (2011) using lidar and field observations. However, the magnitude of our inferred thickness values depend strongly on the model parameters, which need to be calibrated to specific sets of landslides. Regardless of which flow-law parameters are used, the model predicts a highly irregular slide thickness.

We also estimated the basal topography by subtracting the thickness profile from the surface elevation data, and these predictions show that the Boulder Creek earthflow has an irregular basal-slip surface and displays variability over both short (10^2 m) and long (10^3 m) length scales (Fig. 8). Note the basal surface closely mimics the ground-surface topography. We do not have the required borehole measurements or seismic data to test our model predictions, but our first-order analysis agrees well with predictions and observations of a variable slide thickness from other slow-moving landslides around the world (Baum et al., 1993; Coe et al., 2009; Booth et al., 2013a; Guerriero et al., 2014; Prokešová et al., 2014).

6. Discussion

6.1. Geometrical controls on earthflow kinematics

The Eel River earthflows display distinct kinematic zones that can vary significantly in average velocity. By comparing the 13 slides that occur within the lidar data to Mackey and Roering (2011) landslide inventory, we found that the locations of these kinematic zones have remained spatially fixed for almost 70 years. This strongly suggests that landslide geometry exerts a primary control on long-term landslide kinematics. Our results agree well with other studies that have quantified the kinematic history of slow-moving earthflows (e.g., Coe et al., 2009; Guerriero et al.,

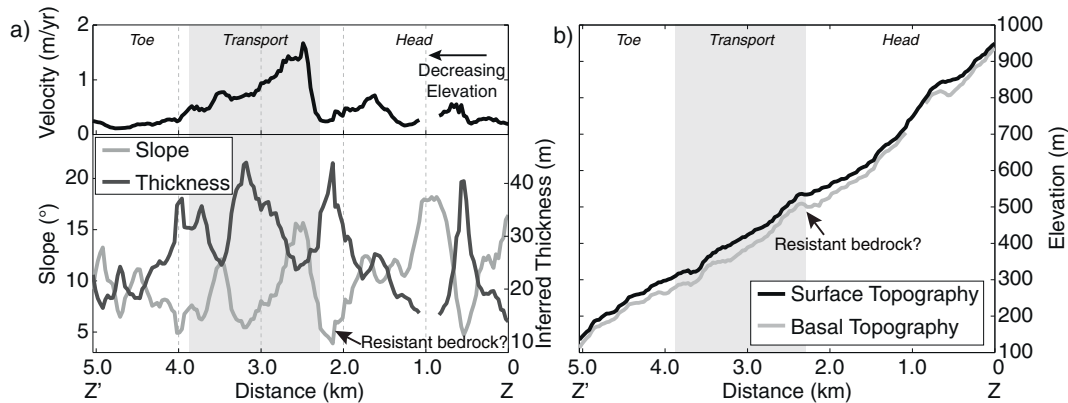


Fig. 8. Topographic slope, velocity, model-inferred thickness, and elevation profiles from Z to Z' along the longitudinal axis of the Boulder Creek earthflow (see profile line in Fig. 4). We set the earthflow density $\rho = 2145 \text{ kg m}^{-3}$, flow-law exponent $p = 3$, and flow-law constant $c = 4.6 \times 10^{-21} \text{ m kg}^{-9} \text{ yr}^{5/3}$. a) Slope, velocity, and model-inferred thickness profiles. Black line corresponds to temporally-averaged (2007–2011) velocity profile projected onto the downslope direction. b) Basal and surface topography profiles. Elevation is given as meters above sea level. Basal topography is calculated by subtracting the surface elevation profile by the inferred thickness. Note the basal surface closely mimics the ground-surface topography. Both display irregularities over short (10^2 m) and large (10^3 m) spatial scales. We have indicated the location of a feature, which we have inferred to be resistant bedrock.

2014). In a recent study on the Montaguto earthflow, Italy, [Guerrero et al. \(2014\)](#) concluded that the positions of the kinematic zones are set by the geometry of the basal-sliding surface. Given our similar results, we propose that the kinematics of the Eel River earthflows is also controlled by the geometry of the basal-sliding surface.

By modeling these earthflows with a viscous non-Newtonian rheology, we were able to infer slide thickness and basal topography along the axis of the Boulder Creek earthflow. Our model results suggest slide thickness and basal topography must vary significantly in order to explain the observed relationships between topographic slope and velocity at the ground surface. We also observed that the inferred basal topography closely mimics the ground surface topography along much of the landslide. We hypothesize that these inferred variations result from structural and lithologic features along the landslide base. It is encouraging that our results agree with studies that have used a variety of methods to infer and measure landslide thickness ([Mizuno, 1989](#); [Baum et al., 1993](#); [Coe et al., 2009](#); [Booth et al., 2013a](#); [Guerrero et al., 2014](#); [Prokešová et al., 2014](#)); however before this method can be widely applied it requires validation through substantial field investigation.

Given that structural and lithologic features remain spatially fixed for long time periods, they can exert significant control on landslide motion as the landslide material is forced to deform in order to slide over these surfaces. These features can influence local groundwater flow and affect pore-water pressures ([Keefer and Johnson, 1983](#); [Iverson and Major, 1987](#); [Baum and Johnson, 1993](#); [Van Asch et al., 2006](#)). For instance, the compression and extension of the landslide colluvium as it deforms over an irregular surface can lead to increases and decreases in pore-water pressures, respectively. Furthermore, these features effect the stress distribution along the sliding surface and within the landslide body ([Mizuno, 1989](#); [Baum and Fleming, 1991](#); [Guerrero et al., 2014](#); [Prokešová et al., 2014](#)).

Many studies have examined the effects of an irregular slip surface on controlling the motion of tectonic faults and glaciers ([Weertman, 1957](#); [Nye, 1969](#); [Chester and Chester, 1978–2012](#); [Dunham et al., 2011](#)). For faults, sliding along an irregular slip-surface produces complex behaviors resulting from variations in normal stress along the surface. These irregularities (i.e. asperities) also increase the surface roughness of the slip surface. Over time, however, the slip surface roughness decreases as subsequent sliding events break off asperities ([Sagy et al., 2007](#)). Like faults, a landslide's slip surface may evolve over long periods of sustained motion. For instance, the preferential development and alignment of clay minerals along the shear zone may act to reduce the surface roughness and alter the mechanical properties of the slip surface ([Bishop et al., 1971](#); [Wang et al., 2010](#)). Yet, it appears that these slope failures are unable to suppress the expression of large asperities, such as those associated with resistant bedrock ([Baum et al., 1993](#); [Coe et al., 2009](#); [Guerrero et al., 2014](#)). One potential example of this type of feature can be observed at the Boulder Creek earthflow near the upper edge of the transport zone ([Fig. 4](#); [Fig. 8](#)). As the Boulder Creek earthflow translates over the upslope edge of this feature, there is a decrease in topographic slope, a predicted increase in slide thickness, and decrease in downslope velocity on the upslope edge; while translation over the downslope edge results in an increase in topographic slope, a predicted decrease in thickness, and an increase in velocity. Thus, this feature appears to have spatially fixed the upslope location of the transport zone.

Although landslide geometry likely controls the long-term motion of the Eel River earthflows, it does not appear to strongly regulate their response to seasonal stress perturbations. Instead, the frictional properties and pore-water pressure along the sliding surface controls the magnitude of those rates. We found that these earthflows exhibit seasonal velocity changes consistent with precipitation-induced changes in effective normal stress. For the four earthflows analyzed in detail, the velocity of the transport zone relative to the toe and head zones scales in proportion and shows no detectable phase lag through the seasonal cycle. This suggests that changes in effective normal stress are communicated along the shear zone within the timescales resolved by our InSAR dataset (i.e. <46 days). Given that these slides are driven by precipitation-induced

changes in pore-water pressure, one explanation is that these patterns of seasonal acceleration and deceleration are triggered by spatially extensive stress perturbations resulting from seasonal changes in groundwater level along the slide body ([Iverson, 1986](#); [Iverson and Major, 1987](#); [Berti and Simoni, 2012](#)). However, it is possible that these earthflows exhibit differences in the timing of motion along the slide body, driven by local stress perturbations, that occur over timescales that are unresolved by the sampling frequency of our InSAR data. [Iverson \(1986\)](#) concluded that the rate at which local stress perturbations travel along the landslide depends on the material properties of the landslide colluvium. If the landslide material exhibits plastic deformation, perturbations progress rapidly and diffuse along the slide body. If the landslide material exhibits viscous deformation, perturbations progress as a slow-moving kinematic wave over the course of several years. The nearby Minor Creek landslide, which likely has similar material properties to our slides, exhibits a combination of plastic- and viscous-like deformation, but is able to respond rapidly to local stress perturbations ([Iverson, 1986](#)). Therefore, in order to identify any potential nonuniform motion requires velocity data with a much higher temporal sampling. Future work includes plans for field monitoring and the use of data from newer satellites that have a shorter repeat intervals (<2 weeks).

7. Conclusion

The Eel River catchment contains many active earthflows that display persistent long-term motion with seasonal variations in velocity. Using satellite InSAR and high-resolution DEMs, we identify 50 active slow-moving landslides over a ~14,000 km² area in the Northern California Coast Ranges. We find no clear relationship between landslide size, average slope, or average velocity. All but one of these landslides occur within the Central and Eastern belts of the Franciscan Complex indicating a strong lithologic control on their spatial distribution. Each slide displays three main kinematic zones that have remained spatially fixed over seasonal and decadal timescales, suggesting that kinematics are primarily controlled by landslide geometry. Modeling earthflow motion using a viscous flow-law constrained by surface kinematics, we find that individual slides likely display significant variations in thickness and an irregular basal-slip surface. These potential variations in the basal-slip surface can be used to explain surface deformation patterns.

Time series analysis of four representative earthflows revealed that each slide, despite significant variations in geometry, exhibited seasonal velocity changes that occur along the entire landslide body. Velocities increased rapidly during the wet season and decreased gradually throughout the dry season. Although each slide displays distinct kinematic zones with different mean velocities, the timing of seasonal motion appears to occur synchronously along the landslide body. This behavior can be explained by two alternate hypotheses: 1) seasonal motion is controlled by spatially extensive changes in effective normal stress, or 2) that local stress perturbations are communicated along the slide body over daily-to-monthly timescales, which cannot be resolved with our InSAR data. Our results suggest that slide geometry controls long-term motion and sets kinematic patterns, but does not strongly regulate their response to seasonal stress perturbations.

Supplementary data to this article can be found online at <http://dx.doi.org/10.1016/j.geomorph.2015.06.003>.

Acknowledgments

SAR data were acquired by JAXA and distributed through WInSAR and ASF (www.asf.alaska.edu/sar-data/insar). Topographic data were provided by USGS (ned.usgs.gov) and NCALM/OpenTopography (www.opentopography.org). Lidar dataset name: Eel River, CA: Landsliding and the Evolution of Mountainous Landscapes. Precipitation data from Richardson Grove State Park, CA is provided by NOAA (www.ncdc.noaa.gov). This work was supported by NASA grant 10-ESI10-0010 and NNX08AF95G to JJR and DAS. Editor T. Oguchi and two anonymous

reviewers provided helpful comments. We thank Adam Booth, Ben Mackey, and Bill Schulz for sharing data and for insightful discussions. Lastly, we thank Kirill Trapeznikov for help with coding and data visualization.

Appendix A. Projecting LOS velocity onto the downslope sliding direction

A.1. Methodology

To directly compare landslides to each other and to the historic landslide record (Mackey and Roering, 2011), we back-projected the LOS velocity onto the downslope sliding direction using a straightforward vector manipulation. First, we define the unit look vector in the direction of the satellite LOS

$$\hat{l}_{sat} = \cos(\gamma) \sin(\theta) \hat{n} + \sin(\gamma) \sin(\theta) \hat{e} + \cos(\theta) \hat{z} \tag{A.1}$$

where \hat{l}_{sat} is the unit look vector, γ (with units of degrees) defines the orientation of the look vector in the horizontal plane from North, θ is the look angle from nadir, and \hat{n} , \hat{e} , and, correspond to the North, East, and vertical components, respectively. These values are taken directly from the ALOS PALSAR satellite parameter file. Next, we define the unit vector for the downslope sliding direction for each landslide.

$$\hat{h}_{ls} = \cos(\zeta) \sin(90-\alpha) \hat{n} + \sin(\zeta) \sin(90-\alpha) \hat{e} + \cos(90-\alpha) \hat{z} \tag{A.2}$$

where \hat{h}_{ls} is the downslope direction unit vector, the angle ζ defines the orientation of the downslope direction (i.e., azimuth) in the horizontal plane from North, and the angle α is the average slope angle. To measure

ζ and α , we use the DEM and the horizontal orientation derived from tree-vector motion (Mackey and Roering, 2011). We find that the downslope vector direction closely matches the direction of steepest descent along the slide axis. Then we calculate the downslope velocity at a given pixel i .

$$V_i = \Delta\phi_i (\hat{l}_{sat} \cdot \hat{h}_{ls})^{-1} \tag{A.3}$$

where V_i is the downslope velocity and $\Delta\phi_i$ is the LOS velocity. To avoid projection errors, we only project the LOS velocity onto the downslope direction in areas where we have high quality measurements to constrain the downslope azimuth and hillslope angle.

A.2. Limits of the LOS viewing geometry

As mentioned in Section 5.1, InSAR cannot detect surface deformation that occurs along the satellite’s flight path. Therefore, we are unable to measure landslide motion along hillslopes and landslides that have a poor viewing geometry, and along individual landslides that display changes in downslope direction along the length of the landslide.

To show the effects of the viewing geometry on measurements of landslide motion, we present a case study at the Kekawaka Creek 1 (Kw1) earthflow (Fig. A1). The Kw1 earthflow displays an almost 90° change in direction transitioning from the transport to toe zone. This change in direction results in a switch from ground motion away from the satellite (positive range change, red color) to motion towards the satellite (blue color), and we observe no deformation when the landslide motion crosses the orientation of the satellite’s flight path.

We also calculated a synthetic example to further emphasize how the direction of ground motion affects our ability to detect landslide

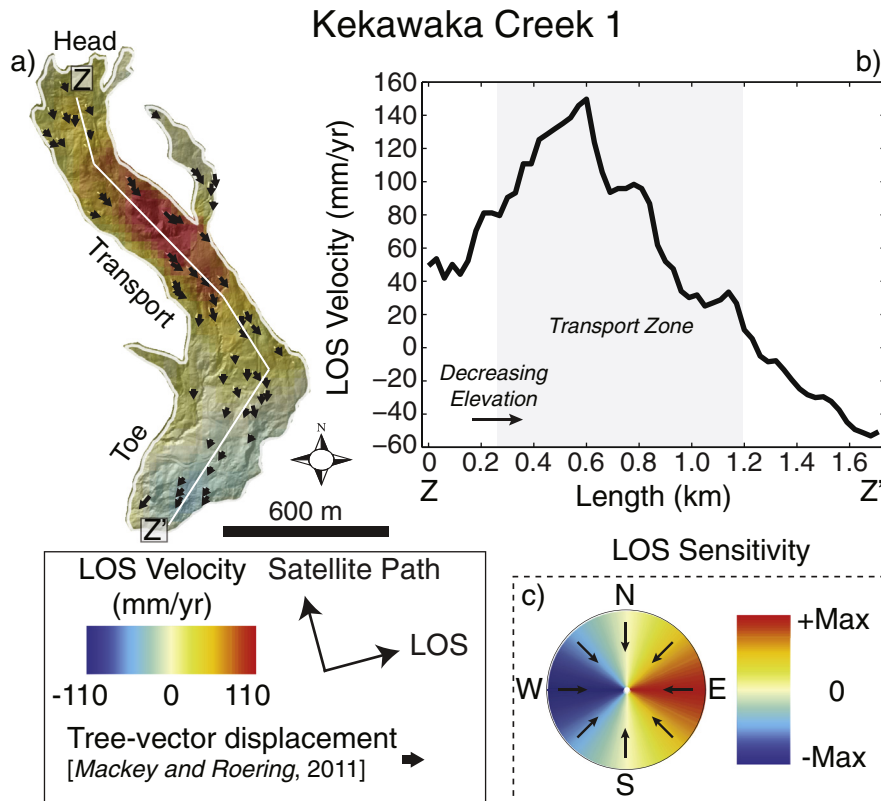


Fig. A1. Limits of the line-of-sight (LOS) viewing geometry. a) 4-year averaged interferogram draped over lidar hillshade map. Positive velocity values correspond to motion away from the satellite along the line-of-sight. The color scales are saturated such that the actual velocity values (mm yr^{-1}) exceeded the maximum and minimum listed values. Black vectors show landslide motion mapped using historic aerial photos (Mackey and Roering, 2011). White solid line indicates location of velocity profile shown in b). Slide is delineated into head, transport, and toe zone. b) Profile from Z to Z' showing LOS velocity (mm yr^{-1}). Shaded area in b) marks the spatial location of the transport zone. Note the change from negative LOS velocity (motion away from satellite), to zero velocity, to positive LOS velocity (motion towards satellite) as landslide changes downslope direction. c) Synthetic example to show how the direction of ground motion affects observed landslide displacement. Compass plot shows how changes in landslide aspect from 0 to 360° (where 0° is North) influence the theoretically measured LOS velocity. (For interpretation of the references to color in this figure legend, the reader is referred to the web version of this article.)

displacement (Fig. A1c). Our synthetic example is constructed using an idealized landslide that has a constant slope α and velocity V . We then vary the landslide's direction of motion ζ and rearrange Eq. (A.3) to project displacement onto the satellite's LOS.

$$\Delta\phi_i(\zeta) = V(\hat{I}_{\text{sat}} \cdot \hat{h}_i(\zeta)) \quad (\text{A.4})$$

The compass plot shows how changes in hillslope aspect from 0 to 360° (where 0° is North) influence the theoretically measured LOS velocity.

References

- Balco, G., Finnegan, N., Gendaszek, A., Stone, J.O., Thompson, N., 2013. Erosional response to northward-propagating crustal thickening in the coastal ranges of the US Pacific Northwest. *Am. J. Sci.* 313, 790–806.
- Baum, R.L., Fleming, R.W., 1991. Use of longitudinal strain in identifying driving and resisting elements of landslides. *Geol. Soc. Am. Bull.* 103, 1121–1132.
- Baum, R.L., Johnson, A.M., 1993. Steady movement of landslides in fine-grained soils: a model for sliding over an irregular slip surface. *US Geol. Surv. Bull.* 1842, 28 pp. (USA).
- Baum, R.L., Reid, M.E., 1995. Geology, hydrology, and mechanics of a slow-moving, clay-rich landslide, Honolulu, Hawaii. *Rev. Eng. Geol.* 10, 79–106.
- Baum, R.L., Fleming, R.W., Johnson, A.M., 1993. Kinematics of the Aspen Grove Landslide, Ephraim Canyon, Central Utah.
- Berti, M., Simoni, A., 2010. Field evidence of pore pressure diffusion in clayey soils prone to landsliding. *J. Geophys. Res. Earth Surf.* 2003–2012, 115.
- Berti, M., Simoni, A., 2012. Observation and analysis of near-surface pore-pressure measurements in clay-shales slopes. *Hydrol. Process.* 26, 2187–2205.
- Bishop, K.M., 1999. Determination of translational landslide slip surface depth using balanced cross sections. *Environ. Eng. Geosci.* 5, 147–156.
- Bishop, A.W., Green, G., Garga, V., Andresen, A., Brown, J., 1971. A new ring shear apparatus and its application to the measurement of residual strength. *Geotechnique* 21, 273–328.
- Booth, A.M., Roering, J.J., 2011. A 1-D mechanistic model for the evolution of earthflow-prone hillslopes. *J. Geophys. Res. Earth Surf.* 116. <http://dx.doi.org/10.1029/2011JF002024>.
- Booth, A.M., Lamb, M.P., Avouac, J.P., Delacourt, C., 2013a. a. Landslide velocity, thickness, and rheology from remote sensing: La Clapière landslide, France. *Geophys. Res. Lett.* 40, 4299–4304.
- Booth, A.M., Roering, J.J., Rempel, A.W., 2013b. b. Topographic signatures and a general transport law for deep-seated landslides in a landscape evolution model. *J. Geophys. Res. Earth Surf.* 118, 603–624.
- Bovis, M.J., Jones, P., 1992. Holocene history of earthflow mass movements in South-Central British Columbia: the influence of hydroclimatic changes. *Can. J. Earth Sci.* 29, 1746–1755.
- Brown, W.M., Ritter, J.R., 1971. Sediment Transport and Turbidity in the Eel River Basin. California: U.S. Geological Survey Water-Supply Paper 1986 67 p.
- Bürgmann, R., Hilley, G., Ferretti, A., Novali, F., 2006. Resolving vertical tectonics in the San Francisco Bay area from permanent scatterer InSAR and GPS analysis. *Geology* 34, 221–224.
- Calabro, M., Schmidt, D., Roering, J., 2010. An examination of seasonal deformation at the Portuguese bend landslide, Southern California, using radar interferometry. *J. Geophys. Res. Earth Surf.* 2003–2012, 115.
- Castañeda, C., Gutiérrez, F., Manunta, M., Galve, J.P., 2009. Dinsar measurements of ground deformation by sinkholes, mining subsidence, and landslides, Ebro River, Spain. *Earth Surf. Process. Landf.* 34, 1562–1574.
- Chester, F.M., Chester, J.S., 1978–2012. Stress and deformation along wavy frictional faults. *J. Geophys. Res. Solid Earth* 105, 23421–23430.
- Coe, J.A., Ellis, W.L., Godt, J.W., Savage, W.Z., Savage, J.E., Michael, J., Kibler, J.D., Powers, P.S., Lidke, D.J., Debray, S., 2003. Seasonal movement of the slumgullion landslide determined from global positioning system surveys and field instrumentation, July 1998–March 2002. *Eng. Geol.* 68, 67–101.
- Coe, J.A., McKenna, J.P., Godt, J.W., Baum, R.L., 2009. Basal-topographic control of stationary ponds on a continuously moving landslide. *Earth Surf. Process. Landf.* 34, 264–279.
- Colesanti, C., Wasowski, J., 2006. Investigating landslides with space-borne synthetic aperture radar (SAR) interferometry. *Eng. Geol.* 88, 173–199.
- Dunham, E.M., Belanger, D., Cong, L., Kozdon, J.E., 2011. Earthquake ruptures with strong-late-weakening friction and off-fault plasticity, part 2: nonplanar faults. *Bull. Seismol. Soc. Am.* 101, 2308–2322.
- Farr, T.G., Rosen, P.A., Caro, E., Crippen, R., Duren, R., Hensley, S., Kobrick, M., Paller, M., Rodriguez, E., Roth, L., et al., 2007. The shuttle radar topography mission. *Rev. Geophys.* 45.
- Ferretti, A., Prati, C., Rocca, F., 2001. Permanent scatterers in sar interferometry. *Geosci. Remote Sens. IEEE Trans.* 39, 8–20.
- Fuller, T.K., Perg, L.A., Willenbring, J.K., Lepper, K., 2009. Field evidence for climate-driven changes in sediment supply leading to strath terrace formation. *Geology* 37, 467–470.
- Furlong, K.P., Govers, R., 1999. Ephemeral crustal thickening at a triple junction: the Mendocino crustal conveyor. *Geology* 27, 127–130.
- Gesch, D., Oimoen, M., Greenlee, S., Nelson, C., Steuck, M., Tyler, D., 2002. The national elevation dataset. *Photogramm. Eng. Remote. Sens.* 68, 5–32.
- Goldstein, R.M., Werner, C.L., 1998. Radar interferogram filtering for geophysical applications. *Geophys. Res. Lett.* 25, 4035–4038.
- Guerriero, L., Coe, J.A., Revellino, P., Grelle, G., Pinto, F., Guadagno, F.M., 2014. Influence of slip-surface geometry on earth-flow deformation, Montaguto earth flow, Southern Italy. *Geomorphology* 219, 285–305. <http://dx.doi.org/10.1016/j.geomorph.2014.04.039>.
- Handwerger, A.L., Roering, J.J., Schmidt, D.A., 2013. Controls on the seasonal deformation of slow-moving landslides. *Earth Planet. Sci. Lett.* 377, 239–247.
- Haneberg, W.C., 1991. Pore pressure diffusion and the hydrologic response of nearly saturated, thin landslide deposits to rainfall. *J. Geol.* 886–892.
- Hilley, G.E., Bürgmann, R., Ferretti, A., Novali, F., Rocca, F., 2004. Dynamics of slow-moving landslides from permanent scatterer analysis. *Science* 304, 1952–1955.
- Hungr, O., 1995. A model for the runout analysis of rapid flow slides, debris flows, and avalanches. *Can. Geotech. J.* 32, 610–623.
- Hungr, O., Evans, S., Bovis, M., Hutchinson, J., 2001. A review of the classification of landslides of the flow type. *Environ. Eng. Geosci.* 7, 221–238.
- Hutchinson, J.N., 1970. A coastal mudflow on the London clay cliffs at Beltinge, North Kent. *Geotechnique* 20, 412–438.
- Iverson, R.M., 1986. Unsteady, nonuniform landslide motion: 2. Linearized theory and the kinematics of transient response. *J. Geol.* 349–364.
- Iverson, R.M., 2005. Regulation of landslide motion by dilatancy and pore pressure feedback. *J. Geophys. Res. Earth Surf.* 2003–2012, 110.
- Iverson, N.R., 2010. Shear resistance and continuity of subglacial till: hydrology rules. *J. Glaciol.* 56, 1104–1114.
- Iverson, R.M., Major, J.J., 1987. Rainfall, ground-water flow, and seasonal movement at Minor Creek landslide, Northwestern California: physical interpretation of empirical relations. *Geol. Soc. Am. Bull.* 99, 579–594.
- Jayko, A., Blake, M., McLaughlin, R., Ohlin, H., Ellen, S., Kelsey, H., 1989. Reconnaissance geologic map of the covelo 30-by 60-minute quadrangle. Northern California: US Geological Survey Miscellaneous Field Investigation Map MF-2001, scale 1, 000.
- Jennings, C.W., Strand, R.G., Rogers, T.H., 1977. Geologic Map of California: 1969–1973. Division of Mines and Geology.
- Keefer, D.K., Johnson, A.M., 1983. Earth Flows: Morphology, Mobilization, and Movement. United States Government Printing Office.
- Kelsey, H.M., 1978. Earthflows in Franciscan Melange, Van Duzen River Basin, California. *Geology* 6, 361–364.
- Larsen, I.J., Montgomery, D.R., Korup, O., 2010. Landslide erosion controlled by hillslope material. *Nat. Geosci.* 3, 247–251.
- Lock, J., Kelsey, H., Furlong, K., Woolace, A., 2006. Late neogene and quaternary landscape evolution of the Northern California Coast Ranges: evidence for mendocino triple junction tectonics. *Geol. Soc. Am. Bull.* 118, 1232–1246.
- Lohman, R.B., Simons, M., 2005. Some thoughts on the use of insar data to constrain models of surface deformation: noise structure and data downsampling. *Geochem. Geophys. Geosyst.* 6.
- Lowry, B., Gomez, F., Zhou, W., Mooney, M., Held, B., Grasmick, J., 2013. High resolution displacement monitoring of a slow velocity landslide using ground based radar interferometry. *Eng. Geol.* 166, 160–169.
- Mackey, B.H., Roering, J.J., 2011. Sediment yield, spatial characteristics, and the long-term evolution of active earthflows determined from airborne lidar and historical aerial photographs, Eel River, California. *Geol. Soc. Am. Bull.* 123, 1560–1576.
- Mackey, B., Roering, J., McKean, J., 2009. Long-term kinematics and sediment flux of an active earthflow, Eel River, California. *Geology* 37, 803–806.
- Mackey, B.H., Roering, J.J., Lamb, M.P., 2011. Landslide-dammed paleolake perturbs marine sedimentation and drives genetic change in anadromous fish. *Proc. Natl. Acad. Sci.* 108, 18905–18909.
- Malet, J.P., Maquaire, O., Calais, E., 2002. The use of global positioning system techniques for the continuous monitoring of landslides: application to the super-sauze earthflow (Alpes-De-Haute-Provence, France). *Geomorphology* 43, 33–54.
- McLaughlin, R.J., Ellen, S.D., Blake, M.C.J., Jayko, A.S., Irwin, W.P., Aalto, K.R., Carver, G.A., Clark, S.H.J., 2000. Geology of the Cape Mendocino, Eureka, Garberville, and Southwestern Part of the Hayfork 30 × 60 Minute Quadrangles and Adjacent Offshore Area. Northern California: U.S. Geological Survey Miscellaneous Field Studies Map MF-2336, 1:100 000 scale.
- Merritts, D., Bull, W.B., 1989. Interpreting quaternary uplift rates at the Mendocino triple junction, Northern California, from uplifted marine terraces. *Geology* 17, 1020–1024.
- Mizuno, K., 1989. Landsliding of clayey slopes with a wavy slip surface: model and its application. Science reports of the Institute of Geoscience, University of Tsukuba. Section A., *Geogr. Sci.* 10, 87–151.
- Nye, J., 1969. A calculation on the sliding of ice over a wavy surface using a Newtonian viscous approximation. *Proceedings of the Royal Society of London. A. Math. Phys. Sci.* 311, 445–467.
- Priest, G.R., Schulz, W.H., Ellis, W.L., Allan, J.A., Niem, A.R., Niem, W.A., 2011. Landslide stability: role of rainfall-induced, laterally propagating, pore-pressure waves. *Environ. Eng. Geosci.* 17, 315–335.
- Prokešová, R., Kardoš, M., Táborsk, P., Medvedová, A., Stacke, V., Chudy, F., 2014. Kinematic behaviour of a large earthflow defined by surface displacement monitoring, dem differencing, and ert imaging. *Geomorphology* 224, 86–101.
- Reid, M.E., 1994. A pore-pressure diffusion model for estimating landslide-inducing rainfall. *J. Geol.* 709–717.
- Roering, J.J., Stimely, L.L., Mackey, B.H., Schmidt, D.A., 2009. Using dinsar, airborne lidar, and archival air photos to quantify landsliding and sediment transport. *Geophys. Res. Lett.* 36.
- Roering, J.J., Mackey, B.H., Handwerger, A.L., Booth, A.M., Schmidt, D.A., Bennett, G.L., Cerovski-Darriau, C., 2015. Beyond the angle of repose: a review and synthesis of

- landslide processes in response to rapid uplift, Eel River, Northern California. *Geomorphology* 236, 109–131.
- Rosen, P.A., Hensley, S., Peltzer, G., Simons, M., 2004. Updated repeat orbit interferometry package released. *Eos, Trans. Am. Geophys. Union* 85, 47.
- Sagy, A., Brodsky, E.E., Axen, G.J., 2007. Evolution of fault-surface roughness with slip. *Geology* 35, 283–286.
- Scheingross, J.S., Minchew, B.M., Mackey, B.H., Simons, M., Lamb, M.P., Hensley, S., 2013. Fault-zone controls on the spatial distribution of slow-moving landslides. *Geol. Soc. Am. Bull.* 125, 473–489.
- Schmidt, D.A., Bürgmann, R., 2003. Time-dependent land uplift and subsidence in the Santa Clara Valley, California, from a large interferometric synthetic aperture radar data set. *J. Geophys. Res. Solid Earth* 1978–2012, 108.
- Schulz, W.H., Kean, J.W., Wang, G., 2009a. a. Landslide movement in Southwest Colorado triggered by atmospheric tides. *Nat. Geosci.* 2, 863–866.
- Schulz, W.H., McKenna, J.P., Kibler, J.D., Biavati, G., 2009b. b. Relations between hydrology and velocity of a continuously moving landslide—evidence of pore-pressure feedback regulating landslide motion? *Landslides* 6, 181–190.
- Schulz, W., Coe, J., Shurtleff, B., Panosky, J., Farina, P., Ricci, P., Barsacchi, G., 2012. Kinematics of the slumgullion landslide revealed by ground-based insar surveys. *Landslides and Engineered Slopes: Protecting Society through Improved Understanding—Proc. of the 11th International and 2nd North American Symposium on Landslides and Engineered Slopes*, pp. 1273–1279.
- Simoni, A., Ponza, A., Picotti, V., Berti, M., Dinelli, E., 2013. Earthflow sediment production and Holocene sediment record in a large apennine catchment. *Geomorphology* 188, 42–53.
- Stimely, L.L., 2009. Characterizing Landslide Movement at the Boulder Creek Earthflow, Northern California, Using L-band InSAR (Ph.D. thesis). University of Oregon.
- Swanson, F.J., Swanston, D.N., 1977. Complex mass-movement terrains in the Western Cascade range, Oregon. *Rev. Eng. Geol.* 3, 113–124.
- Terzaghi, K., 1951. Mechanism of landslides. Department of Engineering. Harvard University.
- Tong, X., Sandwell, D., Smith-Konter, B., 2013. High-resolution interseismic velocity data along the san andreas fault from GPS and InSAR. *J. Geophys. Res. Solid Earth* 118, 369–389.
- Van Asch, T.W., Malet, J.P., Van Beek, L., 2006. Influence of landslide geometry and kinematic deformation to describe the liquefaction of landslides: some theoretical considerations. *Eng. Geol.* 88, 59–69.
- Van Genuchten, P., De Rijke, H., 1989. On pore water pressure variations causing slide velocities and accelerations observed in a seasonally active landslide. *Earth Surf. Process. Landf.* 14, 577–586.
- Vulliet, L., Hutter, K., 1988. Viscous-type sliding laws for landslides. *Can. Geotech. J.* 25, 467–477.
- Wang, G., Suemine, A., Schulz, W.H., 2010. Shear-rate-dependent strength control on the dynamics of rainfall-triggered landslides, Tokushima Prefecture, Japan. *Earth Surf. Process. Landf.* 35, 407–416.
- Weertman, J., 1957. On the sliding of glaciers. *J. Glaciol.* 3, 33–38.
- Wei, M., Sandwell, D., Smith-Konter, B., 2010. Optimal combination of InSAR and GPS for measuring interseismic crustal deformation. *Adv. Space Res.* 46, 236–249.
- Wheatcroft, R., Sommerfield, C., 2005. River sediment flux and shelf sediment accumulation rates on the Pacific Northwest Margin. *Cont. Shelf Res.* 25, 311–332.
- Zhao, C., Lu, Z., Zhang, Q., de la Fuente, J., 2012. Large-area landslide detection and monitoring with ALOS/PALSAR imagery data over Northern California and Southern Oregon, USA. *Remote Sens. Environ.* 124, 348–359.